Design of Novel Transition-Metal-Doped C_6N_2 with High-Efficiency Polysulfide Anchoring and Catalytic Performances toward Application in Lithium−Sulfur Batteries

Cheng He, Yu Liang, and Wenxue Zhang*

Cite This: ACS Appl. Mater. Interfaces 2022, 14, 29120−29130   Read Online

ACCESS | Metrics & More | Article Recommendations | Supporting Information

ABSTRACT: Lithium−sulfur (Li−S) batteries are highly expected because of their high theoretical specific capacity and energy density. However, its application still faces challenges, including the shuttle effect affecting the sulfur reduction reaction, the high decomposition energy barrier of Li_2S during charging, the volume change of sulfur, and the poor conductivity during charging and discharging. Here, combined with density functional theory and particle swarm optimization algorithm for the nitrogen carbide monolayer structural search ($C_mN_{8−m}$, $m = 1−8$), the surprising discovery is that a single metal-atom-doped C_6N_2 monolayer could effectively accelerate the conversion of lithium polysulfide and anchor lithium polysulfide during discharging and decrease the decomposition energy barrier of Li_2S during charging. This "anchoring and catalyzing" mechanism

effectively reduces the shuttle effect and greatly improves the reaction kinetics. Among a series of metal atoms, Cr is the best doping element, and it exhibits suitable adsorption energy for polysulfides and the lowest decomposition energy barrier for Li_2S. This work opens up a new way for the development of transition-metal-doped carbon−nitrogen materials with an excellent catalytic activity for lithium polysulfide as cathode materials for Li−S batteries.

KEYWORDS: lithium−sulfur batteries, transition-metal-doped C_6N_2, adsorption, catalytic oxidation, first-principles calculation
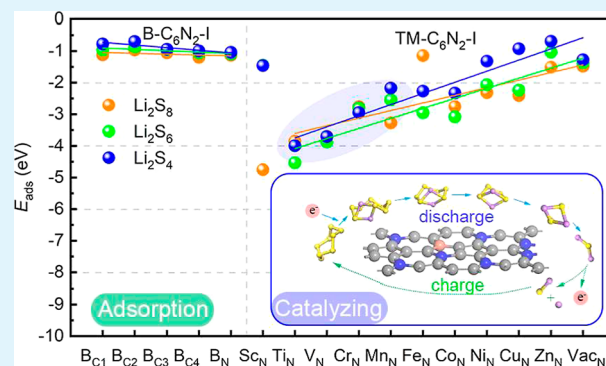
1. INTRODUCTION

To meet the increasing global energy storage demand, lithium−sulfur (Li−S) batteries can be used as a substitute for rechargeable batteries in the future due to their high theoretical capacity (1675 mA h g$^{−1}$) and energy density (2600 W h kg$^{−1}$), except for the low cost, nontoxicity, and earth abundance of sulfur.[1−4] However, some existing challenges have hindered the commercialization of Li−S batteries. One of them is the "shuttle effect" caused by the dissolution of high-order lithium polysulfides (LiPSs), which results in the partial loss of the active electrode and the formation of an insulation layer on the cathode, inducing the disturbance of the sulfur reduction reaction (SRR) in the discharge process and the reduction of the capacity and coulombic efficiency of Li−S batteries. Second, the reaction energy barrier of Li_2S (full discharge product) decomposition in the first step of the charging process is high, which is not conducive to the conversion of LiPSs in the charging reaction. In addition, the volume change of sulfur is more than 80% after full discharge, and the electronic conductivity of sulfur and its lithium products is poor, causing difficulty in the charging and discharging process.[2,5,6] These existing challenges hinder the performance improvement of Li−S batteries.

Some carbon-containing materials have pores or an interlayer space, which is conducive to the physical limitation of LiPSs, and thus, using carbon-containing materials as electrodes is one of the most effective methods to solve these problems,[2] including porous carbon,[7] carbon nanotubes,[8] and carbon nanofibers.[9,10] Although carbon-containing materials have the advantages of an extremely low molecular weight, a good conductivity and stability, the weak interaction between nonpolar carbon-containing materials and polar LiPSs makes LiPSs easy to detach from the surface. LiPSs further diffuse into the electrolyte, causing capacity attenuation.[11] Hence, some heteroatoms (such as boron, nitrogen, sulfur, transition metal (TM), or co-doping) are introduced into carbonaceous materials to form polar functional groups to enhance the immobilization of LiPSs on the electrode.[12−15] For example, Zheng et al. confirmed that C_3N_4 and C_2N can capture LiPSs
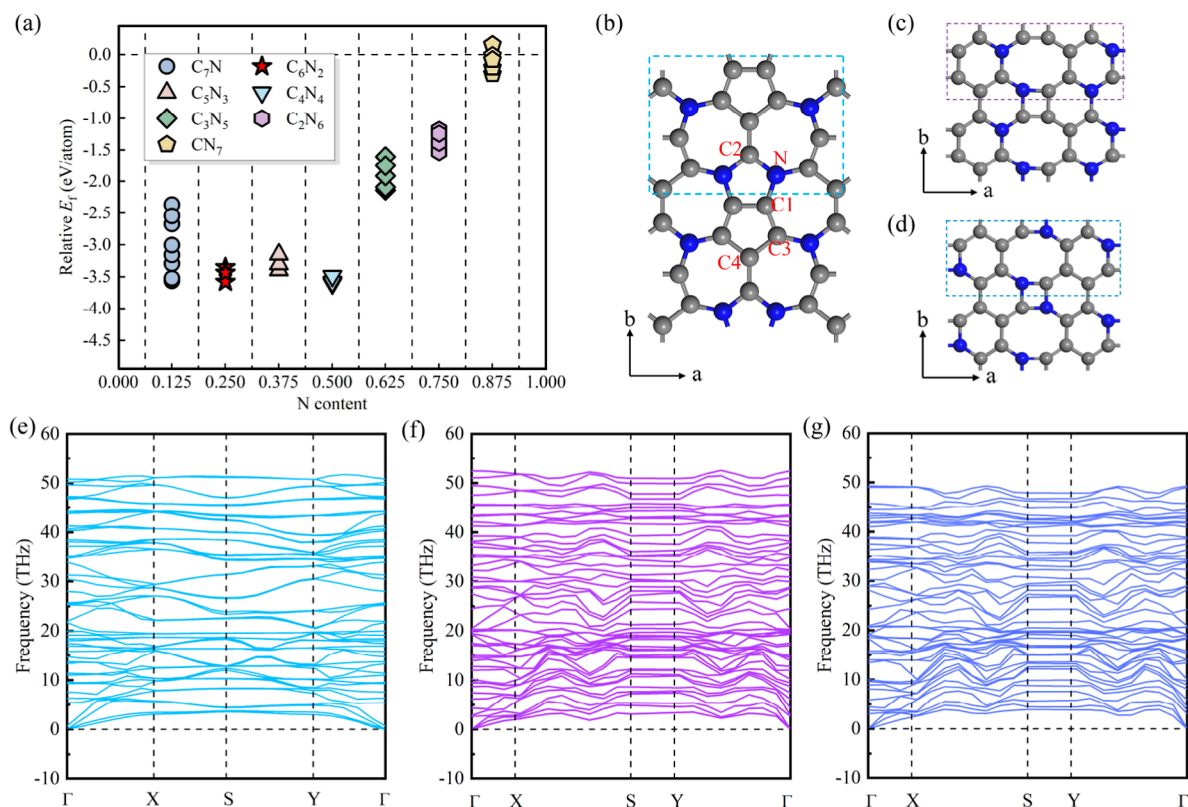
Figure 1. (a) Relative formation energies of C_mN_{8-m} ($m = 1-8$) monolayers with respect to C and N atoms at 0 K. Three structural models for the C_6N_2 monolayer: (b) C_6N_2-I, (c) C_6N_2-II, and (d) C_6N_2-III (the C and N atoms are denoted by gray and blue balls, respectively). Phonon band structures for the C_6N_2 monolayer: (e) C_6N_2-I, (f) C_6N_2-II, and (g) C_6N_2-III.

by enhancing the interfacial interaction and alleviate the interaction of LiPSs with solvents and subsequent dissolution.[16] Zhang et al. confirmed that B/N-doped graphene/ MoX_2 (X = S and Se) exhibits excellent anchoring properties for soluble LiPSs since B/N doping significantly improves the electrical conductivity and changes the surface properties of the carbon material.[17] Recently, there have also been many experimental studies on heteroatom-doped carbon materials as cathode, such as P-doped carbon foam,[18] N/S co-doped porous carbon nanofibers,[19] pyridinic nitrogen doped carbon nanoflakes,[20] and so forth. Since nonmetal atoms have fewer electrons, the adsorption energy of high-order LiPSs on the substrate formed by nonmetal-doped carbon materials is small (only 1.0−1.5 eV),[21,22] which is not enough to effectively suppress the shuttle effect. Therefore, the modification effect of doping with metal atoms with more d orbital electrons is more effective. Moreover, doping one metal atom on carbonaceous materials can modify the electronic structure and catalyze some reactions, which is called a single-atom catalyst (SAC). The SAC is a new type of heterogeneous catalyst with exposed active metal atoms attached to the carrier. Owing to its high catalytic activity and the highest metal utilization rate, the SAC has broad application prospects in the field of catalysis, such as the hydrogen evolution reaction,[23] nitrogen reduction reaction,[24] oxygen reduction reaction,[25,26] and so forth. Significantly, this catalytic material is more conducive to expediting redox kinetics and improving the performance of Li−S batteries through the "anchoring and catalyzing" mechanism.[27,28] The SAC can accelerate the kinetic rate of the SRR and Li_2S decomposition reaction and enable long-life and high-energy Li−S batteries.[29] There are many carbon−

nitrogen materials doped with TM atoms to form SACs, such as C_2N doped with TM atoms,[30] TM phthalocyanines (TiPc),[31] and so forth, which are used as cathodes. Consequently, it is necessary to design the required cathode, such as a carbon−nitrogen material doped with one single metal atom, to meet the requirements for electrode materials with suitable adsorption capacities and catalytic activities, which combine the catalysis of SAC and the porous advantages of carbon−nitrogen materials.

Herein, through particle swarm optimization (PSO) algorithm,[32] an extensive structure search for eight different stoichiometry nitrogen carbide (C_mN_{8-m}, $m = 1-8$) monolayers were conducted. Among them, the C_6N_2 monolayer was selected based on its small relative formation energy, excellent electrical conductivity, and suitable adsorption performance to LiPSs. Then, one nitrogen atom on the C_6N_2 monolayer is selected as the most stable doping site for TM (TM = Sc, Ti, V, Cr, Mn, Fe, Co, Ni, Cu, and Zn) atom, and 10 different monolayers are constructed. We investigate their adsorption strength, catalytic SRR, and Li_2S decomposition to evaluate the anchoring and catalytic performance. It is found that doping Ti, V, Cr, or Mn atoms is conducive to enhancing the anchoring and catalytic performance of the C_6N_2 monolayer. Among them, Cr is the best doping element. Cr-doped C_6N_2 has a suitable adsorption energy and the best catalysis of SRR and Li_2S decomposition, and its electrical conductivity could also be well-maintained during cycling.

2. COMPUTATIONAL METHODS

All calculations, including structural optimization and electronic properties, were performed in the Vienna Ab initio Simulation

Table 1. Elastic Constants (C_{11}, C_{22}, C_{12}, and C_{66}, in N/m), Young's Modulus (Y_x, Y_y: the Y Value along the x, y Direction, in N/m), and Poisson's Ratio (ν_x, ν_y) of the Stable C_6N_2 Monolayers (C_6N_2-I, C_6N_2-II, and C_6N_2-III)

system	C_{11} (N/m)	C_{22} (N/m)	C_{12} (N/m)	C_{66} (N/m)	Y_x (N/m)	Y_y (N/m)	ν_x	ν_y
C_6N_2-I	357.751	326.947	65.555	126.849	344.607	314.934	0.201	0.183
C_6N_2-II	335.877	266.841	81.550	126.664	310.954	247.041	0.306	0.243
C_6N_2-III	308.155	260.886	77.233	123.235	285.291	241.529	0.296	0.251

Package (VASP) with the projector augmented wave method.[33,34] The electron exchange−correlation interaction was described by the Perdew−Burke−Ernzerhof (PBE)[35] functional within the generalized gradient approximation.[36] Because the PBE function will always underestimate the band gap value, the HSE06 hybrid function was more suitable to obtain more accurate electric property calculations.[37] The cutoff energy for the plane-wave-basis set was set to 400 eV. In the constructed two-dimensional (2D) single-layer material structure, a 20 Å vacuum layer was established to avoid the influence of the periodic structure. A Monkhorst−Pack grid of 4 × 4 × 1 was used to sample the first Brillouin zone. In all adsorption systems, the DFT-D3 correction method was adopted to accurately calculate the interaction between monolayers and S_8/Li_2S_x (x = 1, 2, 4, 6, and 8) species,[38,39] and the energy convergence condition for structural optimization was set to 1×10^{-4} eV between two iterated steps. Molecular dynamics (MD) simulations were performed using the *NVT* ensemble and COMPASS force field to investigate the dynamic stability.

The calculated adsorption energy (E_{ads}) is adopted to evaluate the adsorption strength between S_8/LiPSs and the substrate in vacuum. E_{ads} is given as

$$E_{ads} = E_{LiPSs/substrate} - E_{substrate} - E_{LiPSs} \qquad (1)$$

where $E_{LiPSs/substrate}$, $E_{substrate}$, and E_{LiPSs} are the total energies of the polysulfides adsorbed system, isolate substrate, and S_8/LiPSs in vacuum.

The solvent effects were considered by using the implicit solvent model. The commonly used organic electrolyte solvent in Li−S batteries is DOL (1,3-dioxane)/DME (1,2-dimethoxyalkane) (1:1, v/v), so the dielectric constant was set to 7.17. The adsorption energy (E_{ads}^{sol}) of S_8/LiPSs in the solvent is given by the following formula

$$E_{ads}^{sol} = E_{LiPSs/substrate}^{sol} - E_{substrate}^{sol} - E_{LiPSs}^{sol} \qquad (2)$$

where $E_{LiPSs/substrate}^{sol}$, $E_{substrate}^{sol}$, and E_{LiPSs}^{sol} are the total energies of the polysulfides adsorbed system, isolate substrate and S_8/LiPSs in solvent, respectively.

3. RESULTS AND DISCUSSION

3.1. Structures of C_6N_2 and the Adsorption Performance.
PSO is adopted to extensively search for eight stoichiometric nitrogen carbide (C_mN_{8-m}, m = 1−8) monolayers. As shown in Figure 1a, the relative formation energy is calculated to determine their relative stability. C_7N, C_6N_2, and C_4N_4, which have higher C/N ratios, have lower formation energies and are relatively stable. Many previous studies have also investigated more thermodynamically stable configurations with different C/N ratios, such as $C_{1-x}N_x$ (0 < x < 1),[40] C_3N,[41] and so forth. The carbon−nitrogen materials with stable configurations all have a high C/N ratio, which is consistent with our research results. Except for stability, electrical conductivity is essential to the cathode material of Li−S batteries. Our previous studies have shown that C_7N and C_4N_4 monolayers are both semiconductors with band gaps of 0.64 and 0.68 eV (Figure S1), respectively, while C_6N_2 has a better electrical conductivity.[42,43] Therefore, the system of C_6N_2 is the best choice for the cathode material of Li−S batteries, and the different isomers of C_6N_2 are all selected for the further analysis.

In the C_6N_2 system with identified N content, there are three different configurations with stable structures, which are marked as C_6N_2-I, C_6N_2-II, and C_6N_2-III, as shown in Figure 1b−d. The unit cell parameters are a = 7.31 and b = 5.76 Å for C_6N_2-I, a = 9.89 and b = 4.35 Å for C_6N_2-II and a = 9.97 and b = 4.38 Å for C_6N_2-III. To predict the experimental feasibility of the three C_6N_2 monolayers, the cohesive energy (E_{coh}) is calculated as follows[42,44]

$$E_{coh} = \frac{E_{C_6N_2} - xE_C - yE_N}{x + y} \qquad (3)$$

where $E_{C_6N_2}$, E_C, and E_N are the total energies of the C_6N_2 monolayer, isolated C and N atoms, respectively, and x and y represent the numbers of C and N atoms in the primitive cell. According to eq 3, the E_{coh} values of C_6N_2-I, C_6N_2-II, and C_6N_2-III are calculated to be −6.996, −6.862, and −6.939 eV/cell, respectively, so C_6N_2-I is the most feasible experimentally. In addition, to prove the structural stabilities of C_6N_2-I, C_6N_2-II, and C_6N_2-III, the phonon vibration frequencies are calculated, as shown in Figure 1e−g. There is no imaginary frequency in the phonon spectrums of C_6N_2-I, C_6N_2-II, and C_6N_2-III, indicating that the structures of the three C_6N_2 monolayers are thermodynamically stable. Moreover, to further prove their structural thermodynamic stability, MD simulations are performed lasting 1 ns at 300, 400, and 500 K. Figure S2a−c shows the trend of energy over time, and the three atomic structures of C_6N_2-I, C_6N_2-II, and C_6N_2-III lasting 1 ns at 500 K. It is found that the three structures have no obvious deformation, and the energy fluctuations are small, which further proves the thermodynamic stability. Furthermore, to evaluate the mechanical stabilities, the elastic constants of C_6N_2-I, C_6N_2-II, and C_6N_2-III are calculated, as shown in Table 1. The elastic constants of a mechanically stable 2D material must obey the Born criteria: $C_{11}C_{22} - C_{12}^2 > 0$ and $C_{66} > 0$.[45] Therefore, the elastic constants of C_6N_2-I, C_6N_2-II, and C_6N_2-III satisfy the Born criteria, demonstrating their mechanical stabilities.

Moreover, the electronic structures of C_6N_2-I, C_6N_2-II, and C_6N_2-III are further calculated, and the band structures are shown in Figure S3. C_6N_2-I has a metallic property, while C_6N_2-II and C_6N_2-III are both semiconductors with 0.93 and 0.11 eV, respectively. Previous studies have suggested that because the S_8 cathode itself has a poor conductivity, a kind of 2D material with electrical conductivity is more suitable for the cathode of Li−S batteries.[46] Herein, C_6N_2-I is thus mainly considered as an electrode material.

Next, we will explore the adsorption properties of C_6N_2-I, C_6N_2-II, and C_6N_2-III. Because the shuttle effect can be restrained by effectively anchoring LiPSs on the cathode, the cathode material should have suitable E_{ads} with LiPSs. Because smaller E_{ads} cannot effectively anchor LiPSs and larger E_{ads} can cause the structure of LiPSs to be destroyed. In Li−S batteries, Li_2S_x (x = 1, 2, 4, 6, 8) clusters are regarded as typical intermediate products of different lithiation stages during

discharging. High-order Li_2S_x (x = 4, 6, 8) are soluble in the electrolyte leading to the shuttle effect, while low-order Li_2S_x (x = 1, 2) are insoluble. Therefore, we take the high-order Li_2S_x (x = 4, 6, 8) as representatives and first explore the adsorption strength between the pristine C_6N_2 monolayers (C_6N_2-I, C_6N_2-II, and C_6N_2-III) and Li_2S_x (x = 4, 6, 8). In Figure S4, different orientations of soluble Li_2S_x (x = 4, 6, 8) on three monolayers are fully optimized. As shown in Table 2,

Table 2. Adsorption Energy (E_{ads}) of Soluble Li_2S_x (x = 4, 6, 8), and Distance (d) between Li_2S_x (x = 4, 6, 8) and C_6N_2-I, C_6N_2-II, C_6N_2-III

system		Li_2S_8	Li_2S_6	Li_2S_4
C_6N_2-I	E_{ads} (eV)	−1.097	−0.990	−0.783
	d (Å)	2.066	2.048	2.403
C_6N_2-II	E_{ads} (eV)	−1.075	−0.934	−0.784
	d (Å)	2.105	2.081	2.455
C_6N_2-III	E_{ads} (eV)	−0.919	−0.823	−0.682
	d (Å)	2.203	2.186	2.234

the E_{ads} of Li_2S_x (x = 4, 6, 8) on C_6N_2-I, C_6N_2-II, and C_6N_2-III are in the range of 0.682−1.097 eV, and the adsorption distances are in the range of 2.048−2.455 Å. The calculated results suggest that the adsorption strengths of Li_2S_x (x = 4, 6, 8) on the pristine C_6N_2 monolayers are very weak, mainly due to the contribution of vdW physical interactions. However, the E_{ads} of soluble Li_2S_x (x = 4, 6, 8) species on the original three C_6N_2 monolayers is equivalent to that of Li_2S_x (x = 4, 6, 8)

species and the commonly used solvents modules (DME or DOL) (E_{ads} = 0.77−0.85 eV). Consequently, the three original C_6N_2 monolayers cannot effectively fix soluble Li_2S_x (x = 4, 6, 8), which indicates that their anchoring performances are unsatisfactory. Nevertheless, since C_6N_2-I has the most negative E_{coh} and E_{ads} of Li_2S_x (x = 4, 6, 8), doping heteroatoms on C_6N_2-I are considered to enhance the polarity of the nitrogen carbide material to enhance its adsorption performance.

3.2. Structures of the B-Doped C_6N_2 Monolayer and Adsorption Performance. Since the B atom has a small atomic radius and fewer electrons, it is an element that is often adopted to modify the surface. Here, the five positions N, C1, C2, C3, and C4, as shown in Figure 1b, are replaced by one B atom, marked as B_N, B_{C1}, B_{C2}, B_{C3}, and B_{C4}. To evaluate the effects of the five doping sites, the E_{coh} values of B_N, B_{C1}, B_{C2}, B_{C3}, and B_{C4} are calculated. For one B-doped system, E_{coh} is given by the following formula

$$E_{coh} = \frac{E_{B-C_6N_2} - xE_C - yE_N - E_B}{x + y + 1} \quad (4)$$

where E_C, E_N, and E_B are the energies of isolated C, N, and B atoms, $E_{B-C_6N_2}$ is the total energy of C_6N_2 doped by one B atom, and x and y represent the number of C and N atoms in the primitive cell. According to the calculated E_{coh} results shown in Table S1, B_N has the most negative E_{coh} of −7.065 eV/atom. In addition, the E_{ads} of Li_2S_x (x = 4, 6, 8) adsorbed on B_N, B_{C1}, B_{C2}, B_{C3}, and B_{C4} should also be considered, as
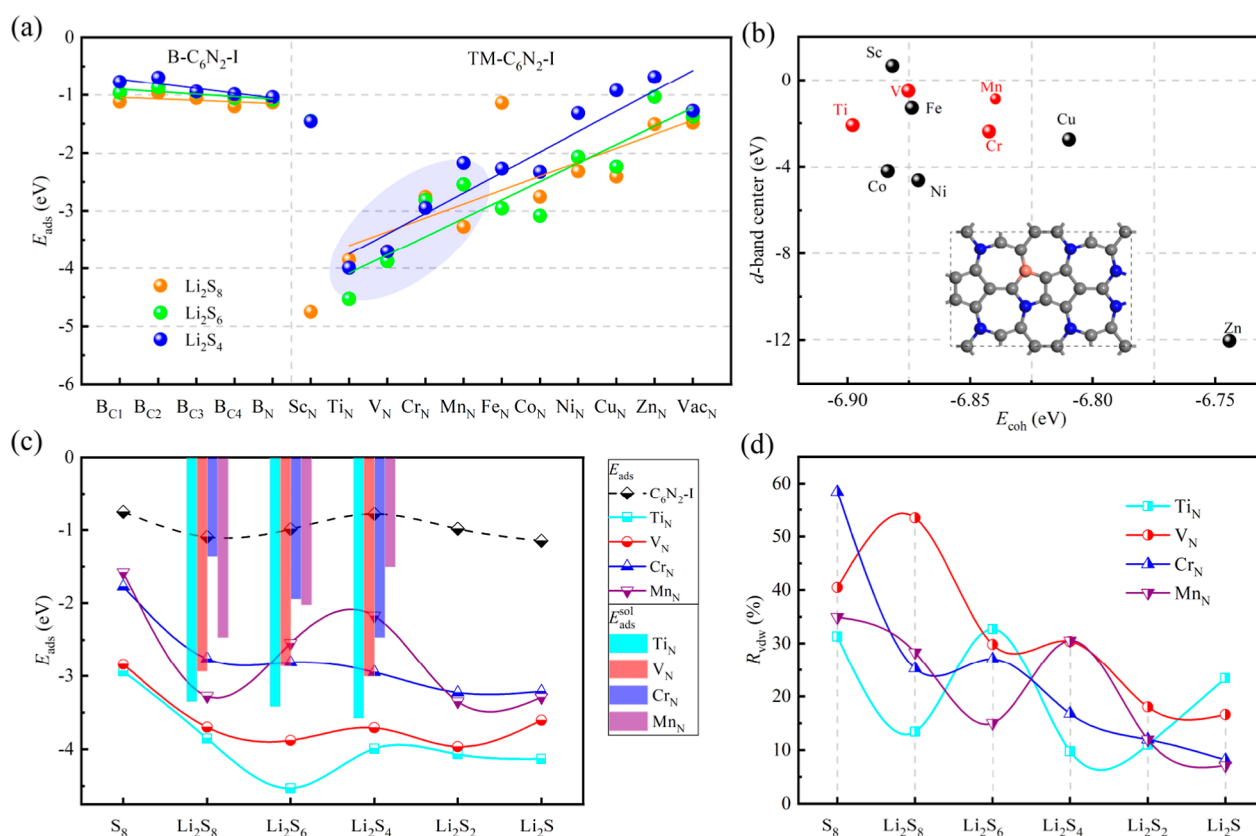

Figure 2. (a) Calculated adsorption energies of soluble Li_2S_8, Li_2S_6, and Li_2S_4 clusters on B/TM-doped/defective C_6N_2-I monolayers; (b) Ashby plot of the d-band center vs cohesion energy of TM_N. (c) E_{ads} of S_8/Li_2S_x (x = 1, 2, 4, 6, 8) on TM_N (TM = Ti, V, Cr, and Mn) in vacuum (solid line) and soluble Li_2S_x (x = 4, 6, 8) on TM_N (TM = Ti, V, Cr, and Mn) in the solvent (columns). (d) Ratio of vdW interactions in E_{ads} of S_8/Li_2S_x (x = 1, 2, 4, 6, 8) on TM_N (TM = Ti, V, Cr, and Mn).

Table 3. Adsorption Energy (E_{ads}) in Vacuum, Bader Charge Analysis (ΔQ), Ratio of van der Waals Interactions, and Adsorption Energy (E_{ads}^{sol}) in the Solvent of S_8/Li_2S_x (x = 1, 2, 4, 6, 8) on TM_N (TM = Ti, V, Cr, and Mn)

system		S_8	Li_2S_8	Li_2S_6	Li_2S_4	Li_2S_2	Li_2S
Ti_N	E_{ads} (eV)	−2.939	−3.854	−4.531	−3.992	−4.069	−4.131
	ΔQ (e^-)	0.944	0.952	0.729	0.821	0.795	−0.387
	R_{vdW}	31.30%	13.43%	32.70%	9.78%	11.00%	23.41%
	E_{ads}^{sol} (eV)		−3.342	−3.409	−3.566		
V_N	E_{ads} (eV)	−2.836	−3.699	−3.878	−3.707	−3.964	−3.604
	ΔQ (e^-)	0.802	0.549	0.699	0.591	0.625	−0.438
	R_{vdW}	40.47%	53.45%	29.82%	31.60%	18.04%	16.62%
	E_{ads}^{sol} (eV)		−2.929	−2.853	−2.997		
Cr_N	E_{ads} (eV)	−1.774	−2.760	−2.810	−2.947	−3.228	−3.213
	ΔQ (e^-)	0.735	0.728	0.603	0.486	0.296	−0.428
	R_{vdW}	58.43%	25.27%	27.04%	16.80%	11.98%	8.16%
	E_{ads}^{sol} (eV)		−1.362	−1.942	−2.463		
Mn_N	E_{ads} (eV)	−1.580	−3.275	−2.545	−2.174	−3.351	−3.292
	ΔQ (e^-)	0.596	0.745	0.696	−0.034	0.589	−0.503
	R_{vdW}	34.92%	28.32%	15.02%	30.56%	11.98%	7.14%
	E_{ads}^{sol} (eV)		−2.462	−2.022	−1.505		

shown in the left part of Figure 2a, and Figure S5 shows the corresponding adsorption configurations. B_N has the highest E_{ads} for Li_2S_x (x = 4, 6, 8) in the range of 1.0−1.2 eV, while B_{C1}, B_{C2}, B_{C3}, and B_{C4} have smaller E_{ads} for Li_2S_x (x = 4, 6, 8) in the range of 0.6−1.2 eV. The distances between Li_2S_x (x = 4, 6, 8) clusters and the monolayers are also relatively large, and there is almost no chemical bond formation between Li_2S_x (x = 4, 6, 8) and B-doped monolayers. It is noticed that after B_{C2} adsorbs Li_2S_6 clusters, a Li−N bond is formed, but E_{ads} is only −0.873 eV. The Li−N bond may not be a real "chemical" bond but is attributed to electrostatic dipole−dipole interactions.[47,48] Through the analysis of the E_{ads} of B doped at five sites, doping with the B atom failed to significantly increase the E_{ads} of the C_6N_2-I monolayer. Nevertheless, by screening the doping sites with B atoms, we found that substituting one B atom for the N site helps to enhance the interaction between heteroatoms and Li_2S_x clusters. Therefore, in the following research, the N sites are doped with other heteroatoms to screen out the most suitable doped heteroatoms.

3.3. Structures of the TM-Doped C_6N_2 Monolayer and Adsorption Performance. Because TM atoms have more d-orbital electrons, they are mostly used to modify the surface to enhance the catalytic or adsorption performance. After the above discussion on B-atom doping, the N-site doping is already selected to form the new monolayers for the TM (TM = Sc, Ti, V, Cr, Mn, Fe, Co, Ni, Cu, and Zn)-doped system, which are marked as Sc_N, Ti_N, V_N, Cr_N, Mn_N, Fe_N, Co_N, Ni_N, Cu_N, and Zn_N below. The doped systems are calculated separately for E_{coh} and the d-band. For TM-doped systems, E_{coh} is given as

$$E_{coh} = \frac{E_{TM-C_6N_2} - xE_C - yE_N - E_{TM}}{x + y + 1} \quad (5)$$

where E_{TM}, E_C, and E_N are the energies of isolated TM, C, and N atoms, $E_{TM-C_6N_2}$ is the total energy of C_6N_2 doped by one TM atom, and x and y represent the number of C and N atoms in the primitive cell. The d-band center is given by[49]

$$C_d = \frac{\int_{-\infty}^{+\infty} E \times PDOS_d(E) \, dE}{\int_{-\infty}^{+\infty} PDOS_d(E) \, dE} \quad (6)$$

According to d-band center theory, there is a good linear relationship between the d-band center and the adsorption energy, so the d-band center energy is used as a "descriptor" to describe the adsorption energy. Materials with the d-band center close to the Fermi level usually have better adsorption and catalytic properties.[50,51] The E_{coh} and d-band center energy of different doping systems are shown in Figure 2b and Table S2. Among the 10 monolayers, Zn_N has relatively small E_{coh}, indicating its low experimental feasibility. In addition, the d-band center values of Co_N, Ni_N, and Zn_N are all less than −4 eV, especially that of Zn_N, which is less than −12 eV, indicating a weaker adsorption performance. Additionally, since the d orbital of Sc_N has only one electron, the adsorption performance of Sc_N is also considered to be poor. As a result, it can be speculated that since the d-band center of several other monolayers (Ti_N, V_N, Cr_N, Mn_N, Fe_N, and Cu_N) are closer to the Fermi level, they have better adsorption properties.

The E_{ads} of adsorption of Li_2S_x (x = 4, 6, 8) after doping TM (TM = Sc, Ti, V, Cr, Mn, Fe, Co, Ni, Cu, and Zn) atoms in the N site of C_6N_2-I are studied as a preliminary screening of metal atoms. In addition, in order to facilitate the study of the effect of metal atoms, we also set up an N vacancy, and the substrate material formed is labeled Vac_N. As shown in the right part of Figure 2a, the E_{ads} of Li_2S_x (x = 4, 6, 8) decreases as the atomic number of TM increases. This changing trend is roughly consistent with the calculated result of the d-band center energy. Figures S6, S7, and 3 show the adsorption configurations of Li_2S_x (x = 4, 6, 8) on TM_N (TM = Sc, Ti, V, Cr, Mn, Fe, Co, Ni, Cu, and Zn). A previous study demonstrated that the formed strong TM−S bonds between monolayers and Li_2S_x clusters could weaken the Li−S bonds in LiPSs, which will promote SRR during discharging and the decomposition of Li_2S during charging.[31] In the configurations of Li_2S_x (x = 4, 6, 8) on TM_N (TM = Sc, Fe, Ni, Cu, and Zn), there are several systems, such as Li_2S_x (x = 4, 6) on Sc_N, Li_2S_8 on Fe_N, and Li_2S_4 on $Ni_N/Cu_N/Zn_N$, in which TM atoms are far away from Li_2S_x (x = 4, 6, 8) clusters and no TM−S bond forms. In contrast, metal atoms on TM_N (TM = Ti, V, Cr, Mn, and Co) are close to Li_2S_x (x = 4, 6, 8) and form the TM−S bond. However, among the above five monolayers, the d-band center energy of Co_N is −4.2 eV, which is more negative than

that of Ti_N, V_N, Cr_N, and Mn_N. Therefore, comprehensively considering the d-band center, the adsorption configurations and E_{ads} of Li_2S_x ($x = 4, 6, 8$), a preliminary screening of TM is carried out. Next, we will further explore other properties of Ti_N, V_N, Cr_N, and Mn_N.

After that, we further continue to calculate the E_{ads} of S_8/Li_2S_x ($x = 1, 2$) on Ti_N, V_N, Cr_N, and Mn_N. The E_{ads} of Ti_N, V_N, Cr_N, and Mn_N for S_8/Li_2S_x ($x = 1, 2, 4, 6, 8$) are summarized in Figure 2c, and the corresponding values are listed in Table 3. The adsorption configurations are shown in Figure 3a−f (Cr_N)
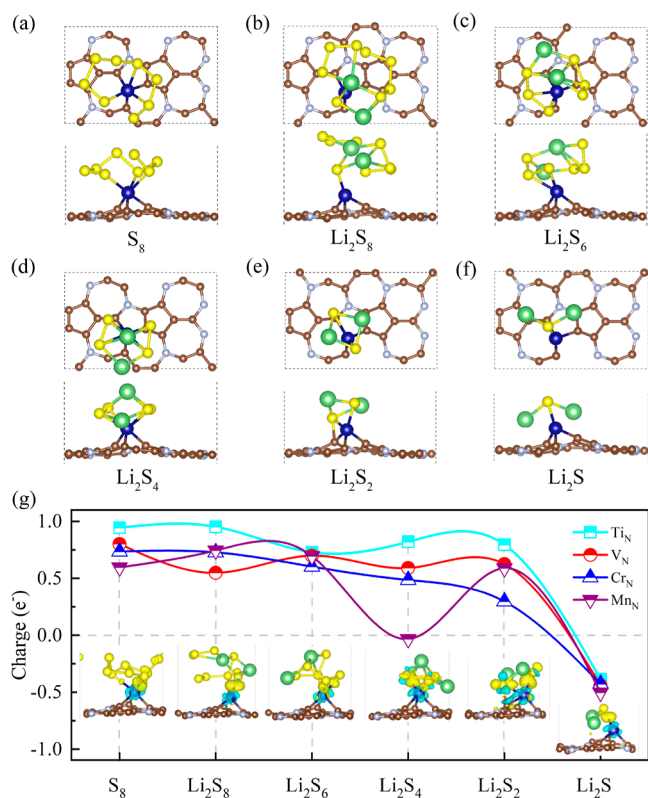
Figure 3. (a−f) Most stable adsorption structures of S_8/Li_2S_x ($x = 1, 2, 4, 6, 8$) on Cr_N with vdW interactions included. (g) Bader charge difference between the adsorbed case and free-standing monolayers (TM_N, TM = Ti, V, Cr, and Mn) at different lithiation stages. The insets show the 3D charge density difference of S_8/Li_2S_x ($x = 1, 2, 4, 6, 8$) on Cr_N with an isovalue of 0.1 e/Å^3. The yellow areas suggest the accumulation of charges, and the blue areas suggest the dissipation of charges.

and Figure S7 (Ti_N, V_N, and Mn_N). The solid line in Figure 2c indicates that the adsorption energies of Ti_N, V_N, Cr_N, and Mn_N of LiPSs increase gradually during the discharge process. In addition, among these four monolayers (Ti_N, V_N, Cr_N, and Mn_N), the E_{ads} of Ti_N and V_N are more negative than the E_{ads} of Cr_N and Mn_N, which indicates that the excessive E_{ads} of Ti_N and V_N may lead to the destruction of the LiPSs structure. For example, S_8 and Li_2S_8 clusters adsorbed on Ti_N and V_N have broken bonds, and their structures are damaged, which is caused by the large E_{ads} of S_8 and Li_2S_8 on Ti_N and V_N. Furthermore, it is noticed that TM−S bonds and Li−N bonds caused by electrostatic dipole−dipole interactions are formed. In summary, the TM−S bond has a significant effect on increasing the adsorption to effectively anchor LiPSs.

In addition, E_{ads}^{sol} of soluble Li_2S_x ($x = 4, 6, 8$) on Ti_N, V_N, Cr_N, and Mn_N in the solvent (DOL/DME) is also calculated to

evaluate the adsorption performances in the solvent, as shown by the columns in Figure 2c and Table 3. The results show that the solvation effect significantly weakens the adsorption strength of Ti_N, V_N, Cr_N, and Mn_N and soluble Li_2S_x ($x = 4, 6, 8$). Similar changes have been found in other related reports.[31] In all adsorption systems, the difference between E_{ads} and E_{ads}^{sol} is not large, so it can be considered that the soluble Li_2S_x ($x = 4, 6, 8$) are anchored by these monolayers and do not dissolve into the electrolyte. Therefore, by introducing appropriate TM atoms, the binding ability of S_8/LiPSs in C_6N_2-I can be well adjusted, including when solvation is considered.

To further analyze the adsorption mechanism of Ti_N, V_N, Cr_N, and Mn_N, the contributions of chemical interactions and physical vdW interactions are estimated at different lithiation stages, as shown in Figure 2d. For the adsorption of S_8, the R_{vdw} of Cr_N is 60%, and the other three are 30−40%. Such smaller values compared with the previous study (80−100%)[21] indicate that TM−S bonds increase the proportion of chemical interactions and adsorb S_8 clusters more firmly. For Li_2S_8, except for V_N, the R_{vdw} of other cases is within 10−30%, so compared to other results,[21,52] the adsorption of Li_2S_8 clusters is stronger, while for Li_2S_x ($x = 2, 4, 6$), R_{vdw} is in the range of 5−35%. In summary, for Ti_N, V_N, Cr_N, and Mn_N, with the progress of the lithiation process, the proportion of the vdW effect gradually decreases, which indicates that the chemical effect gradually takes the main role in the adsorption process, while vdW interaction is dominant in the nonlithiation stage. Therefore, in the nonlithiation stage, the vdW interaction is predominant in the adsorption of S_8, which is conducive to adding Li to form LiPSs and easily migrates to promote SRR. In the lithiation stage, the greater chemical effect means that LiPSs can be effectively anchored to suppress the shuttle effect.

To illustrate the adsorption mechanism between TM atoms and LiPSs, Ti_N, V_N, Cr_N, and Mn_N systems are used to further investigate the charge transfer (ΔQ) after adsorption by Bader charge analysis. A positive ΔQ indicates that electrons transfer from the monolayer to the S_8/LiPSs. As shown in Figure 3g, when the adsorbed clusters are S_8 and Li_2S_x ($x = 2, 4, 6, 8$), the direction of electron transfer is from the monolayer to the cluster. As the number of S atoms in the adsorbed LiPSs species decreases, the amount of electron transfer from the monolayer to the cluster decreases. Even when Li_2S is adsorbed, the direction of the electron transfer is reversed, that is, from the cluster to the monolayer. One reason for the above phenomenon is that after adsorption, S atoms gain electrons, and Li atoms lose electrons. The more S atoms the LiPSs species contains, the more electrons the cluster can obtain. There is also an anomalous example where Li_2S_4 is adsorbed on Mn_N, and the electrons are almost not transferred. Because compared with other systems, the S atoms of Li_2S_4 get fewer electrons. Moreover, it is worth noting that although the eight S atoms in S_8 gain electrons, the E_{ads} of S_8 is still smaller than that of Li_2S_x. This is because S_8 is a stable molecule that is saturated with S atoms, and it is difficult to form strong chemical interactions with TM−S bonds. In addition, the charge density difference of Cr_N is taken as a representative to study the charge transfer between S_8/LiPSs and TM_N. Charge transfer mainly occurs between the TM and S atoms, and its direction is from the TM atom to the S atom. Therefore, the analysis of electronic properties further proved the formation of TM−S bonds when LiPSs are adsorbed.
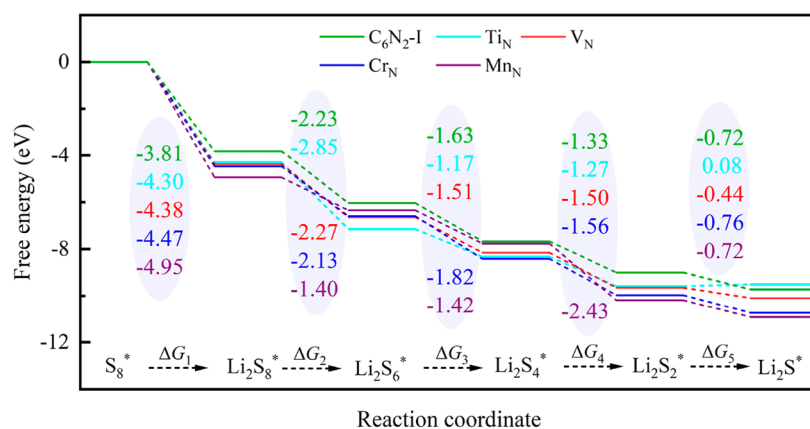
Figure 4. Free-energy profiles for the S_8/Li_2S_x (x = 1, 2, 4, 6, 8) conversion (SRR) on the surface of TM_N (TM = Ti, V, Cr, and Mn) and C_6N_2-I.
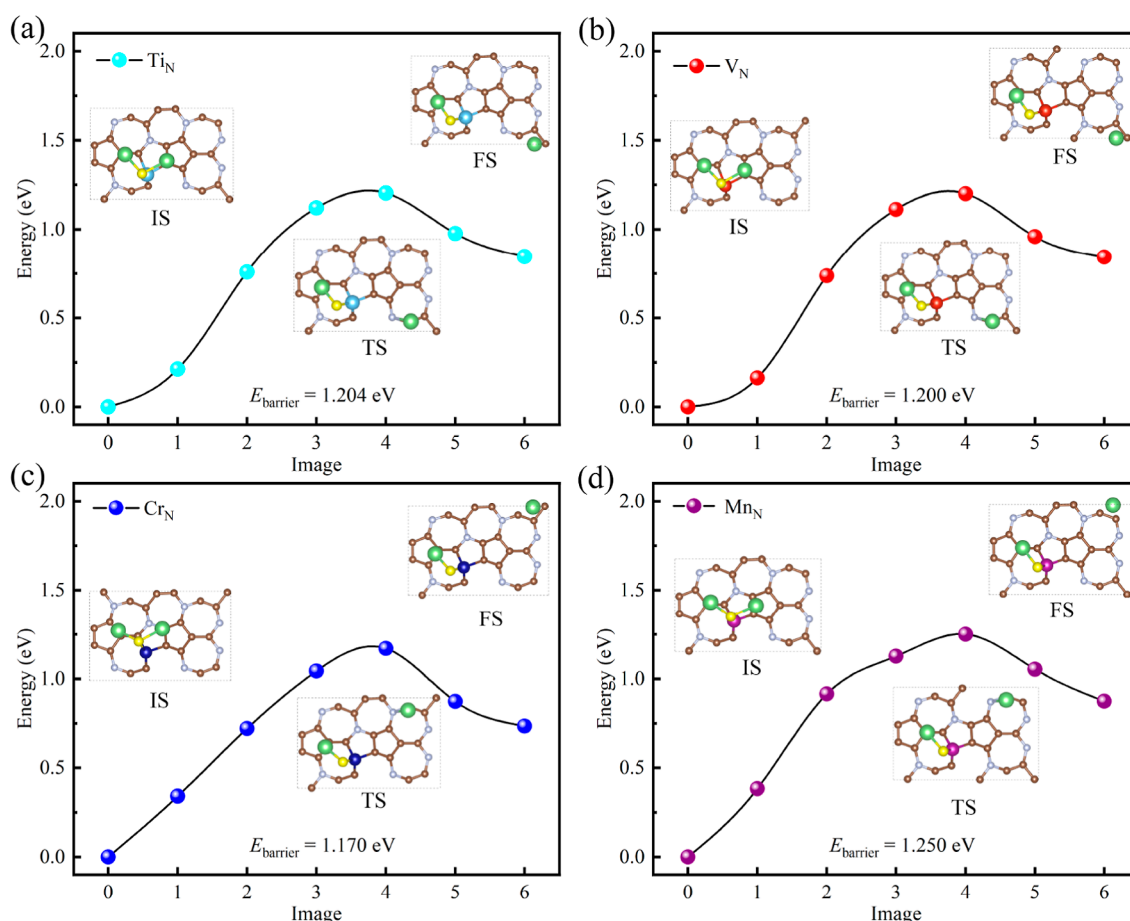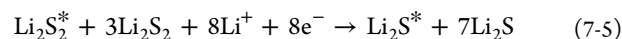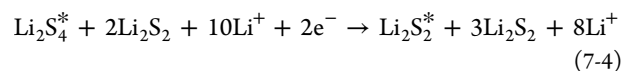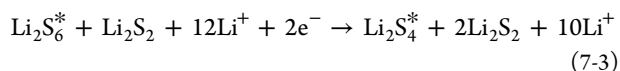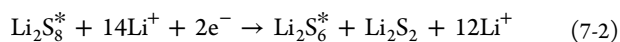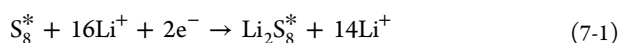

Figure 5. Decomposition energy barriers of the Li_2S adsorbed on (a) Ti_N, (b) V_N, (c) Cr_N, and (d) Mn_N.

3.4. Catalytic SRR and the Li₂S Decomposition Performance.

The shuttle effect hinders the progress of SRR, while an ideal electrode material needs to be able to promote the SRR. Therefore, the catalytic effect of TM_N (TM = Ti, V, Cr, and Mn) on the SRR is studied. The basic steps of SRR to form a Li_2S molecule are[31]

$$S_8^* + 16Li^+ + 2e^- \rightarrow Li_2S_8^* + 14Li^+ \tag{7-1}$$

$$Li_2S_8^* + 14Li^+ + 2e^- \rightarrow Li_2S_6^* + Li_2S_2 + 12Li^+ \tag{7-2}$$

$$Li_2S_6^* + Li_2S_2 + 12Li^+ + 2e^- \rightarrow Li_2S_4^* + 2Li_2S_2 + 10Li^+ \tag{7-3}$$

$$Li_2S_4^* + 2Li_2S_2 + 10Li^+ + 2e^- \rightarrow Li_2S_2^* + 3Li_2S_2 + 8Li^+ \tag{7-4}$$

$$Li_2S_2^* + 3Li_2S_2 + 8Li^+ + 8e^- \rightarrow Li_2S^* + 7Li_2S \tag{7-5}$$

The Gibbs free energies for each elementary reaction step on C_6N_2-I and TM_N (TM = Ti, V, Cr, and Mn) are plotted in Figure 4, and the corresponding information is listed in Table S3. All steps on all monolayers are spontaneously exothermic except for the fifth step of Ti_N. Also, the ΔG_5 of Ti_N is only 0.08 eV. This indicates that the SRR that occurs according to the above reaction pathway is thermodynamically feasible. Compared with other electrode materials,[31,53] C_6N_2-I and
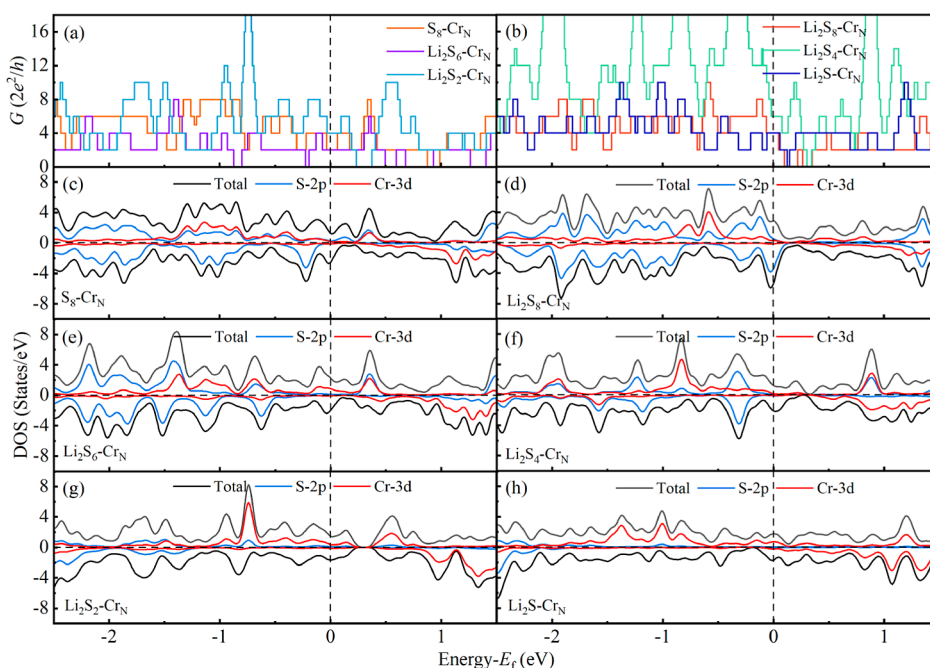
Figure 6. (a,b) G for S_8/Li_2S_x (x = 1, 2, 4, 6, 8)-adsorbed Cr_N. (c)−(h) Density of states (DOS) for S_8/Li_2S_x (x = 1, 2, 4, 6, 8)-adsorbed Cr_N.

TM_N (TM = Ti, V, Cr, and Mn) have the greater advantage that almost all step reactions are exothermic. Therefore, the above several monolayers are more effective in catalyzing SRR.

The first reaction in the charging process is generally considered to be the decomposition of Li_2S into the Li−S radical intermediate and Li-ion ($Li_2S \rightarrow LiS + Li^+ + e^-$).[54] An ideal cathode material needs to catalyze the reaction to maintain the charge−discharge cycle of the Li−S batteries. Herein, Figure 5 shows the calculated decomposition energy barriers of Li_2S on TM_N (TM = Ti, V, Cr, and Mn) surfaces, and the corresponding diffusion paths of one Li atom are shown in Figure S8. The decomposition energy barriers of Li_2S on TM_N (TM = Ti, V, Cr, and Mn) are 1.204, 1.200, 1.170, and 1.250 eV, which are smaller than those of other cathode materials (N/G with 2.29 eV and Co−N/G with 1.43 eV)[55] and the decomposition energy barrier of isolated Li_2S molecules (3.4 eV).[56] Therefore, Cr_N has the smallest decomposition energy barrier of Li_2S, further suggesting that it is a promising candidate as a cathode material for Li−S batteries.

3.5. Volume Change and Conductivity of Electrode Materials. Another challenge for Li−S batteries is the volume change of sulfur during cycling. As shown in Figure S9, by constructing two layers of 2D materials to simulate a three-dimensional periodic structure, the adsorption of S_8 and Li_2S clusters in the middle of the two layers, respectively, indicates before and after discharge. The layer spacing of the two independent Cr_N layers after being completely relaxed is 3.9 Å. Note that after adsorption of the S_8 cluster, the distance between the two monolayers is 7.3 Å, while the distance between the layers after adsorption of Li_2S is 6.4 Å. The volume changed is 12.3% before and after discharging, while the volume change of sulfur itself is more than 80%, indicating that Cr_N as the cathode electrode material of Li−S batteries is beneficial to reducing the volume change of sulfur.

Except for the volume change, the potential cathode material should exhibit excellent conductivity during the charge and discharge process. Hence, it is necessary to calculate the transport and electronic properties of the cathode material after adsorption. To evaluate quantum transport, the quantum conduction (G) function is given as[57]

$$G = G_0 \sum_{M=1}^{M} T_i \tag{8}$$

where $G_0 = 2e^2/h$ is a constant, T_i is the transmission probability of the i th channel, and M is the number of propagating modes crossing the Fermi energy. The more bands that pass through the Fermi energy, the better the conductivity. Figure 6a,b shows the G of S_8 and Li_2S_x (x = 1, 2, 4, 6, 8) adsorbed on Cr_N. Conduction channels appearing near the Fermi level suggest that the conductivity of each adsorption system is higher. Moreover, the spin DOS of S_8- and Li_2S_x-(x = 1, 2, 4, 6, 8)-adsorbed Cr_N is calculated, as shown in Figure 6c−h. Because of the existence of the TM atom, all adsorption systems retain their metallic properties, ensuring the transmission of electrons and the conversion of LiPSs during cycling. The PDOS of the d orbital of the Cr atom and the p orbital of the S atom is also shown in Figure 6. Except for S_8 on Cr_N, the overlap between the p orbitals of S and the d orbitals of Cr in other systems is more obvious below the Fermi level. It is further proven that the formation of TM−S bonds during the adsorption process leads to the improvement of the adsorption performance.

In addition, to further the thermodynamic stability of Cr_N, MD simulations are also performed for Cr_N, and the potential energy versus time curves at 300, 400, and 500 K are shown in Figure S10. The inset is the structure of Cr_N after the simulation at 500 K. The potential energy fluctuation is slightly stronger than that before doping, and the structure is bent, but no structural damage occurs. Therefore, Cr_N has dynamic stability at room temperature. The operating temperature of conventional Li−S batteries is between −20 and 60 °C, indicating that Cr_N can completely maintain the structural stability at the operating temperature of Li−S batteries. In

summary, TM atoms help to modify the surface, and Cr_N is considered to be the most promising electrode material.

4. CONCLUSIONS

In summary, density functional theory calculations have been used to systematically study a series of TM-atom-doped C_6N_2 monolayers as cathode materials for Li−S batteries to inhibit shuttle effect and catalyze the conversion between LiPSs. After Ti, V, Cr, and Mn atom doping with the C_6N_2 monolayer, TM−S bonds are formed between Ti, V, Cr, or Mn and sulfur atoms to improve the adsorption performance between the C_6N_2 monolayers. And the proper adsorption energies could inhibit the shuttle effect while ensuring the integrity of the lithium polysulfide structure. In addition, the presence of Ti, V, Cr, or Mn maintains electrical conductivity during charging and discharging and is conducive to improving the utilization of sulfur. More importantly, the four atoms doping the C_6N_2 monolayer also help to promote the decomposition of Li_2S during charging and the reduction of sulfur during catalytic discharge, which improves the reaction kinetics. Among the four doping schemes, Cr doping is the best because, after Cr doping with the C_6N_2 monolayer, the decomposition energy barrier of Li_2S is the lowest. This work has opened up a new way for the development of a catalytically active carbon−nitrogen cathode material with strong adsorption energy for lithium polysulfide.

ASSOCIATED CONTENT

Supporting Information

The Supporting Information is available free of charge at https://pubs.acs.org/doi/10.1021/acsami.2c07285.

Structure configurations and band structures of C_7N and C_4N_4; MD simulations, band structures of C_6N_2-I, C_6N_2-II, and C_6N_2-III; most stable adsorption structures of soluble Li_2S_x ($x = 4, 6, 8$) on C_6N_2 (C_6N_2-I, C_6N_2-II, C_6N_2-III), B-doped C_6N_2-I (B_N, B_{C1}, B_{C2}, B_{C3}, and B_{C4}), TM-doped C_6N_2-I (Sc_N, Fe_N, Co_N, Ni_N, Cu_N, and Zn_N); most stable adsorption structures of S_8/Li_2S_x ($x = 1, 2, 4, 6, 8$) on Ti_N, V_N, and Mn_N; Li diffusion pathways for Ti_N, V_N, Cr_N, and Mn_N; configuration after complete relaxation of S_8 and Li_2S on Cr_N; and MD simulation of the Cr_N monolayer (PDF)

AUTHOR INFORMATION

Corresponding Author

Wenxue Zhang − *School of Materials Science and Engineering, Chang'an University, Xi'an 710064, China;* ⊙ orcid.org/0000-0002-9327-5761; Email: wxzhang@chd.edu.cn

Authors

Cheng He − *State Key Laboratory for Mechanical Behavior of Materials, School of Materials Science and Engineering, Xi'an Jiaotong University, Xi'an 710049, China*

Yu Liang − *State Key Laboratory for Mechanical Behavior of Materials, School of Materials Science and Engineering, Xi'an Jiaotong University, Xi'an 710049, China*

Complete contact information is available at:
https://pubs.acs.org/10.1021/acsami.2c07285

Notes

The authors declare no competing financial interest.

REFERENCES

(1) Fang, R.; Zhao, S.; Sun, Z.; Wang, D.-W.; Cheng, H.-M.; Li, F. More Reliable Lithium-Sulfur Batteries: Status, Solutions and Prospects. *Adv. Mater.* **2017**, *29*, 1606823.

(2) Yan, R.; Ma, T.; Cheng, M.; Tao, X.; Yang, Z.; Ran, F.; Li, S.; Yin, B.; Cheng, C.; Yang, W. Metal-Organic-Framework-Derived Nanostructures as Multifaceted Electrodes in Metal-Sulfur Batteries. *Adv. Mater.* **2021**, *33*, No. e2008784.

(3) Xu, R.; Lu, J.; Amine, K. Progress in Mechanistic Understanding and Characterization Techniques of Li-S Batteries. *Adv. Energy Mater.* **2015**, *5*, 1500408.

(4) Fan, K.; Ying, Y.; Luo, X.; Huang, H. Nitride MXenes as Sulfur Hosts for Thermodynamic and Kinetic Suppression of Polysulfide Shuttling: A Computational Study. *J. Mater. Chem. A* **2021**, *9*, 25391−25398.

(5) Yang, Y.; Zheng, G.; Cui, Y. Nanostructured Sulfur Cathodes. *Chem. Soc. Rev.* **2013**, *42*, 3018−3032.

(6) Manthiram, A.; Chung, S.-H.; Zu, C. Lithium-Sulfur Batteries: Progress and Prospects. *Adv. Mater.* **2015**, *27*, 1980−2006.

(7) Zhang, J.; Xiang, J.; Dong, Z.; Liu, Y.; Wu, Y.; Xu, C.; Du, G. Biomass Derived Activated Carbon with 3D Connected Architecture for Rechargeable Lithium-Sulfur Batteries. *Electrochim. Acta* **2014**, *116*, 146−151.

(8) Ding, B.; Yuan, C.; Shen, L.; Xu, G.; Nie, P.; Zhang, X. Encapsulating Sulfur into Hierarchically Ordered Porous Carbon as a High-Performance Cathode for Lithium-Sulfur Batteries. *Chem.—Eur. J.* **2013**, *19*, 1013−1019.

(9) Sun, L.; Li, M.; Jiang, Y.; Kong, W.; Jiang, K.; Wang, J.; Fan, S. Sulfur Nanocrystals Confined in Carbon Nanotube Network as a Binder-Free Electrode for High-Performance Lithium Sulfur Batteries. *Nano Lett.* **2014**, *14*, 4044−4049.

(10) Singhal, R.; Chung, S.-H.; Manthiram, A.; Kalra, V. A Free-Standing Carbon Nanofiber Interlayer for High-Performance Lithium-Sulfur Batteries. *J. Mater. Chem. A* **2015**, *3*, 4530−4538.

(11) Zheng, G.; Zhang, Q.; Cha, J. J.; Yang, Y.; Li, W.; Seh, Z. W.; Cui, Y. Amphiphilic Surface Modification of Hollow Carbon Nanofibers for Improved Cycle Life of Lithium Sulfur Batteries. *Nano Lett.* **2013**, *13*, 1265−1270.

(12) Zhang, S. S. Heteroatom-Doped Carbons: Synthesis, Chemistry and Application in Lithium/Sulphur Batteries. *Inorg. Chem. Front.* **2015**, *2*, 1059−1069.

(13) Lin, C. Y.; Zhang, D. T.; Zhao, Z. H.; Xia, Z. H. Covalent Organic Framework Electrocatalysts for Clean Energy Conversion. *Adv. Mater.* **2018**, *30*, 1703646.

(14) Peng, P.; Zhou, Z. H.; Guo, J. N.; Xiang, Z. H. Well-Defined 2D Covalent Organic Polymers for Energy Electrocatalysis. *ACS Energy Lett.* **2017**, *2*, 1308−1314.

(15) Yu, J.; Jin, Y.; Hu, M.; Ren, W.; Xie, Y.; Wang, Y. BC_6N as a Promising Sulfur Host Material for Lithium-Sulfur Batteries. *Appl. Surf. Sci.* **2022**, *577*, 151843.

(16) Zheng, Y.; Li, H.; Yuan, H.; Fan, H.; Li, W.; Zhang, J. Understanding the Anchoring Effect of Graphene, BN, C_2N and C_3N_4 Monolayers for Lithium-Polysulfides in Li-S Batteries. *Appl. Surf. Sci.* **2018**, *434*, 596−603.

(17) Zhang, T.; Wang, H.; Zhao, J. Heterostructures of Doped Graphene and MoX_2 (X = S and Se) as Promising Anchoring

Materials for Lithium-Sulfur Batteries: A First-Principles Study. *New J. Chem.* **2019**, *43*, 9396−9402.

(18) Zou, Y.; Guo, D.; Yang, B.; Zhou, L.; Lin, P.; Wang, J.; Chen, X. A.; Wang, S. Toward High-Performance Lithium-Sulfur Batteries: Efficient Anchoring and Catalytic Conversion of Polysulfides Using P-Doped Carbon Foam. *ACS Appl. Mater. Interfaces* **2021**, *13*, 50093−50100.

(19) Yang, X.; Ran, Z.; Luo, F.; Li, Y.; Zhang, P.; Mi, H. Free-Standing ZIF-8 Derived Nitrogen and Sulfur Co-Doped Porous Carbon Nanofibers Host for High Mass Loading Lithium-Sulfur Battery. *Appl. Surf. Sci.* **2020**, *509*, 145270.

(20) Yuan, H.; Zhang, W.; Wang, J.-G.; Zhou, G.; Zhuang, Z.; Luo, J.; Huang, H.; Gan, Y.; Liang, C.; Xia, Y.; Zhang, J.; Tao, X. Facilitation of Sulfur Evolution Reaction by Pyridinic Nitrogen Doped Carbon Nanoflakes for Highly-Stable Lithium-Sulfur Batteries. *Energy Storage Mater.* **2018**, *10*, 1−9.

(21) Shao, Y.; Wang, Q.; Hu, L.; Pan, H.; Shi, X. BC_2N Monolayers as Promising Anchoring Materials for Lithium-Sulfur Batteries: First-Principles Insights. *Carbon* **2019**, *149*, 530−537.

(22) Qie, Y.; Liu, J.; Wang, S.; Gong, S.; Sun, Q. C_3B Monolayer as an Anchoring Material for Lithium-Sulfur Batteries. *Carbon* **2018**, *129*, 38−44.

(23) Zhang, H.; Yu, L.; Chen, T.; Zhou, W.; Lou, X. W. D. Surface Modulation of Hierarchical MoS_2 Nanosheets by Ni Single Atoms for Enhanced Electrocatalytic Hydrogen Evolution. *Adv. Funct. Mater.* **2018**, *28*, 1807086.

(24) Zhao, J.; Chen, Z. Single Mo Atom Supported on Defective Boron Nitride Monolayer as an Efficient Electrocatalyst for Nitrogen Fixation: A Computational Study. *J. Am. Chem. Soc.* **2017**, *139*, 12480−12487.

(25) Wan, X.; Chen, W.; Yang, J.; Liu, M.; Liu, X.; Shui, J. Synthesis and Active Site Identification of Fe-N-C Single-Atom Catalysts for the Oxygen Reduction Reaction. *ChemElectroChem* **2019**, *6*, 304−315.

(26) Mahmood, J.; Li, F.; Kim, C.; Choi, H.-J.; Gwon, O.; Jung, S.-M.; Seo, J.-M.; Cho, S.-J.; Ju, Y.-W.; Jeong, H. Y.; Kim, G.; Baek, J.-B. $Fe@C_2N$: A Highly-Efficient Indirect-Contact Oxygen Reduction Catalyst. *Nano Energy* **2018**, *44*, 304−310.

(27) Li, B. Q.; Kong, L.; Zhao, C. X.; Jin, Q.; Chen, X.; Peng, H. J.; Qin, J. L.; Chen, J. X.; Yuan, H.; Zhang, Q.; Huang, J. Q. Expediting Redox Kinetics of Sulfur Species by Atomic-Scale Electrocatalysts in Lithium-Sulfur Batteries. *InfoMat* **2019**, *1*, 533−541.

(28) Li, W.; Li, S.; Bernussi, A. A.; Fan, Z. 3-D Edge-Oriented Electrocatalytic $NiCo_2S_4$ Nanoflakes on Vertical Graphene for Li-S Batteries. *Energy Mater. Adv.* **2021**, *2021*, 2712391.

(29) Zhuang, Z.; Kang, Q.; Wang, D.; Li, Y. Single-Atom Catalysis Enables Long-Life, High-Energy Lithium-Sulfur Batteries. *Nano Res.* **2020**, *13*, 1856−1866.

(30) Lin, H.; Jin, R.; Wang, A.; Zhu, S.; Li, H. Transition Metal Embedded C_2N with Efficient Polysulfide Immobilization and Catalytic Oxidation for Advanced Lithium-Sulfur Batteries: A First Principles Study. *Ceram. Int.* **2019**, *45*, 17996−18002.

(31) Yu, B.; He, Q.; Zhao, Y. Exploring the Anchoring Effect and Catalytic Mechanism of 3*d* Transition Metal Phthalocyanine for S_8/LiPSs: A Density Functional Theory Study. *Appl. Surf. Sci.* **2021**, *558*, 149928.

(32) Zhu, L.; Liu, H.; Pickard, C. J.; Zou, G.; Ma, Y. Reactions of Xenon with Iron and Nickel are Predicted in the Earth's Inner Core. *Nat. Chem.* **2014**, *6*, 644−648.

(33) Kresse, G.; Furthmüller, J. Efficient Iterative Schemes for Ab Initio Total-Energy Calculations Using a Plane-Wave Basis Set. *Phys. Rev. B: Condens. Matter Mater. Phys.* **1996**, *54*, 11169−11186.

(34) Kresse, G.; Joubert, D. From Ultrasoft Pseudopotentials to the Projector Augmented-Wave Method. *Phys. Rev. B: Condens. Matter Mater. Phys.* **1999**, *59*, 1758−1775.

(35) Ernzerhof, M.; Scuseria, G. E. Assessment of the Perdew-Burke-Ernzerhof Exchange-Correlation Functional. *J. Chem. Phys.* **1999**, *110*, 5029−5036.

(36) Blöchl, P. E. Projector Augmented-Wave Method. *Phys. Rev. B: Condens. Matter Mater. Phys.* **1994**, *50*, 17953−17979.

(37) Heyd, J.; Scuseria, G. E.; Ernzerhof, M. Hybrid Functionals Based on a Screened Coulomb Potential. *J. Chem. Phys.* **2003**, *118*, 8207−8215.

(38) Grimme, S.; Antony, J.; Ehrlich, S.; Krieg, H. A Consistent and Accurate Ab Initio Parametrization of Density Functional Dispersion Correction (DFT-D) for the 94 Elements H-Pu. *J. Chem. Phys.* **2010**, *132*, 154104.

(39) Grimme, S.; Ehrlich, S.; Goerigk, L. Effect of the Damping Function in Dispersion Corrected Density Functional Theory. *J. Comput. Chem.* **2011**, *32*, 1456−1465.

(40) Bu, S.; Yao, N.; Hunter, M. A.; Searles, D. J.; Yuan, Q. Design of Two-Dimensional Carbon-Nitride Structures by Tuning the Nitrogen Concentration. *npj Comput. Mater.* **2020**, *6*, 128.

(41) Wei, W.; Yang, S.; Wang, G.; Zhang, T.; Pan, W.; Cai, Z.; Yang, Y.; Zheng, L.; He, P.; Wang, L.; Baktash, A.; Zhang, Q.; Liu, L.; Wang, Y.; Ding, G.; Kang, Z.; Yakobson, B. I.; Searles, D. J.; Yuan, Q. Bandgap Engineering of Two-Dimensional C_3N Bilayers. *Nat. Electron.* **2021**, *4*, 486−494.

(42) He, C.; Zhang, M.; Li, T. T.; Zhang, W. X. A Novel C_6N_2 Monolayer as a Potential Material for Charge-Controlled CO_2 Capture. *J. Mater. Chem. C* **2020**, *8*, 6542−6551.

(43) Li, T.; He, C.; Zhang, W. A Novel Porous C_4N_4 Monolayer as a Potential Anchoring Material for Lithium-Sulfur Battery Design. *J. Mater. Chem. A* **2019**, *7*, 4134−4144.

(44) Li, Y.; Liao, Y.; Chen, Z. Be_2C Monolayer with Quasi-Planar Hexacoordinate Carbons: A Global Minimum Structure. *Angew. Chem., Int. Ed.* **2014**, *53*, 7248−7252.

(45) Wang, J.; Yip, S.; Phillpot, S. R.; Wolf, D. Crystal Instabilities at Finite Strain. *Phys. Rev. Lett.* **1993**, *71*, 4182−4185.

(46) Liu, D.; Zhang, C.; Zhou, G.; Lv, W.; Ling, G.; Zhi, L.; Yang, Q.-H. Catalytic Effects in Lithium-Sulfur Batteries: Promoted Sulfur Transformation and Reduced Shuttle Effect. *Adv. Sci.* **2018**, *5*, 1700270.

(47) Hou, T.-Z.; Xu, W.-T.; Chen, X.; Peng, H.-J.; Huang, J.-Q.; Zhang, Q. Lithium Bond Chemistry in Lithium-Sulfur Batteries. *Angew. Chem., Int. Ed.* **2017**, *56*, 8178−8182.

(48) Hou, T.-Z.; Chen, X.; Peng, H.-J.; Huang, J.-Q.; Li, B.-Q.; Zhang, Q.; Li, B. Design Principles for Heteroatom-Doped Nano-carbon to Achieve Strong Anchoring of Polysulfides for Lithium-Sulfur Batteries. *Small* **2016**, *12*, 3283−3291.

(49) Zhang, W.; Cheng, D.; Zhu, J. Theoretical Study of CO Catalytic Oxidation on Free and Defective Graphene-Supported Au-Pd Bimetallic Clusters. *RSC Adv* **2014**, *4*, 42554−42561.

(50) Gao, G.; Waclawik, E. R.; Du, A. Computational Screening of Two-Dimensional Coordination Polymers as Efficient Catalysts for Oxygen Evolution and Reduction Reaction. *J. Catal.* **2017**, *352*, 579−585.

(51) Hammer, B.; Nørskov, J. K. Theoretical Surface Science and Catalysis—Calculations and Concepts. *Adv. Catal.* **2000**, *45*, 71−129.

(52) Jiang, H. R.; Shyy, W.; Liu, M.; Ren, Y. X.; Zhao, T. S. Borophene and Defective Borophene as Potential Anchoring Materials for Lithium-Sulfur Batteries: A First-Principles Study. *J. Mater. Chem. A* **2018**, *6*, 2107−2114.

(53) Song, X.; Qu, Y.; Zhao, L.; Zhao, M. Monolayer Fe_3GeX_2 (X = S, Se, and Te) as Highly Efficient Electrocatalysts for Lithium-Sulfur Batteries. *ACS Appl. Mater. Interfaces* **2021**, *13*, 11845−11851.

(54) Zhou, G.; Tian, H.; Jin, Y.; Tao, X.; Liu, B.; Zhang, R.; Seh, Z. W.; Zhuo, D.; Liu, Y.; Sun, J.; Zhao, J.; Zu, C.; Wu, D. S.; Zhang, Q.; Cui, Y. Catalytic Oxidation of Li_2S on the Surface of Metal Sulfides for Li-S Batteries. *Proc. Natl. Acad. Sci. U.S.A.* **2017**, *114*, 840−845.

(55) Du, Z.; Chen, X.; Hu, W.; Chuang, C.; Xie, S.; Hu, A.; Yan, W.; Kong, X.; Wu, X.; Ji, H.; Wan, L.-J. Cobalt in Nitrogen-Doped Graphene as Single-Atom Catalyst for High-Sulfur Content Lithium-Sulfur Batteries. *J. Am. Chem. Soc.* **2019**, *141*, 3977−3985.

(56) Wang, J.; Jia, L.; Zhong, J.; Xiao, Q.; Wang, C.; Zang, K.; Liu, H.; Zheng, H.; Luo, J.; Yang, J.; Fan, H.; Duan, W.; Wu, Y.; Lin, H.; Zhang, Y. Single-Atom Catalyst Boosts Electrochemical Conversion Reactions in Batteries. *Energy Storage Mater.* **2019**, *18*, 246−252.

(57) Li, T.; He, C.; Zhang, W. Rational Design of Porous Carbon Allotropes as Anchoring Materials for Lithium Sulfur Batteries. *J. Energy Chem.* **2021**, *52*, 121−129.

⧉ Recommended by ACS